Journal of Controlled Release 324 (2020) 644–656

Contents lists available at ScienceDirect

Journal of Controlled Release

journal homepage: www.elsevier.com/locate/jconrel

Glucosamine-NISV delivers antibody across the blood-brain barrier: Optimization for treatment of encephalitic viruses

Stuart Woods[a], Lyn M. O'Brien[b], Wendy Butcher[b], Jane E. Preston[c], Ana R. Georgian[c], E. Diane Williamson[b], F. Javier Salguero[d], Francesca Modino[c], N. Joan Abbott[c], Craig W. Roberts[a], Riccardo V. D'Elia[b,*]

[a] Strathclyde Institute of Pharmacy & Biomedical Sciences, University of Strathclyde, 161 Cathedral Street, Glasgow G4 0RE, UK
[b] Chemical Biological and Radiological Division, Dstl Porton Down, Salisbury SP4 0JQ, UK
[c] Institute of Pharmaceutical Science, King's College London, Franklin-Wilkins Building, 150 Stamford Street, London SE1 9NH, UK
[d] Department of Pathology and Infectious Diseases, School of Veterinary Medicine, University of Surrey, Guildford GU2 7AL, UK

ARTICLE INFO

Keywords:
Non-ionic surfactant vesicle
GLUT1
Glucosamine
Blood-brain barrier
Venezuelan equine encephalitis virus

ABSTRACT

The field of brain drug delivery faces many challenges that hinder development and testing of novel therapies for clinically important central nervous system disorders. Chief among them is how to deliver large biologics across the highly restrictive blood-brain barrier. Non-ionic surfactant vesicles (NISV) have long been used as a drug delivery platform for cutaneous applications and have benefits over comparable liposomes in terms of greater stability, lower cost and suitability for large scale production. Here we describe a glucosamine-coated NISV, for blood-brain barrier GLUT1 targeting, capable of traversing the barrier and delivering active antibody to cells within the brain. *In vitro*, we show glucosamine vesicle transcytosis across the blood-brain barrier with intact cargo, which is partially dynamin-dependent, but is clathrin-independent and does not associate with sorting endosome marker EEA1. Uptake of vesicles into astrocytes follows a more classical pathway involving dynamin, clathrin, sorting endosomes and Golgi trafficking where the cargo is released intracellularly. *In vivo*, glucosamine-coated vesicles are superior to uncoated or transferrin-coated vesicles for delivering cargo to the mouse brain. Finally, mice infected with Venezuelan equine encephalitis virus (VEEV) were successfully treated with anti-VEEV monoclonal antibody Hu1A3B-7 delivered in glucosamine-coated vesicles and had improved survival and reduced brain tissue virus levels. An additional benefit was that the treatment also reduced viral load in peripheral tissues. The data generated highlights the huge potential of glucosamine-decorated NISV as a drug delivery platform with wider potential applications.

1. Introduction

Delivering drugs to the brain is a major challenge, particularly for large molecules and biologics. The restrictive nature of the blood-brain barrier (BBB) prevents all but small (< 450 Da) or lipid soluble drugs from entering the brain, due to a combination of robust tight junctions between capillary endothelia, active multi-drug efflux transport and drug metabolizing enzymes [1]. This is particularly pertinent in the context of this study for delivery of antibodies such as the monoclonal antibody Hu1A3B-7, developed to treat Venezuelan equine encephalitis virus (VEEV) infection [2,3].

One approach is to incorporate drugs within a BBB-permeant nanocarrier to avoid drug efflux transport, shield from metabolism and by-pass restrictive tight junctions. Non-ionic surfactant vesicles (NISVs) have been used as a drug nano-delivery platform since the 1980s. Initially used for cutaneous delivery, they have more recently been employed in chemotherapy, vaccine and gene delivery *via* several routes [4–6]. NISVs have advantages over traditional liposome nanocarriers, showing improved stability, increased drug entrapment, easier sterilization and they are suitable for large scale production [7]. In addition, production methods such as using microfluidization and incorporating membrane stabilizing cholesterol reduces vesicle size and increases cellular drug delivery [7,8].

To improve BBB targeting, NISVs can be functionalised by

Abbreviations: VEEV, Venezuelan equine encephalitis virus; NISV, non-ionic surfactant vesicle; gNISV, glucosamine-coated non-ionic surfactant vesicle; tNISV, transferrin-conjugated non-ionic surfactant vesicle; PBEC, porcine brain endothelial cell

* Corresponding author.
E-mail address: rvdelia@dstl.gov.uk (R.V. D'Elia).

https://doi.org/10.1016/j.jconrel.2020.05.048
Received 19 March 2020; Received in revised form 29 May 2020; Accepted 31 May 2020
Available online 05 June 2020

conjugating ligands that interact with over-expressed BBB transporter or receptor proteins, such as glucose transporter GLUT1 [9], or the transferrin receptor for receptor-mediated transcytosis (RMT) [10]. GLUT1 is greatly enriched at the BBB because of the brain's reliance on glucose as its main energy source. The transporter delivers glucose to the brain at a rate ten-times higher than other tissues, making the brain the main consumer of glucose in the body [11]. NISVs targeting GLUT1 have been used to deliver vasoactive intestinal peptide, doxorubicin and dynorphin B to the brain, using N-palmitoylglucosamine as the ligand [4,12,13]. NISVs targeting transferrin have yet to be used for brain targeting but have been used to deliver hydroxycamptothecin to peripheral tumors [14], and other nanoparticles and liposomes with transferrin conjugation have been shown to successfully deliver a range of drugs to the brain [15].

The urgency for such a formulation is clear in many therapeutic arenas, including the treatment of VEEV. VEEV is a member of the Alphavirus genus and is a positive strand RNA virus (~11.5Kb) with multiple variants (IA/B, IC, ID, IE) [16]. It can cause acute, incapacitating, febrile illness (usually within 2–6 days after infection) and large outbreaks have been recorded including 100,000 cases in Colombia and Venezuela with 300 fatalities [17,18] and a 5% fatality rate in Panama with serotype ID [19]. VEEV causes disease with a very low infectious dose and has multiple exposure routes including aerosol. It is believed to penetrate the brain by olfactory neurone anterograde migration [20] and persists in the brain, which serves as a sanctuary. These facts, along with relative ease of production and previous weaponization, place VEEV as a Category B threat by the Centers for Disease Control. There is also a current lack of licensed prophylaxes or post-exposure therapies for VEEV.

In this study, a key aim was to develop an NISV formulation optimized for BBB targeting and capable of delivering antibody to cells within the brain. NISVs chiefly composed of monopalmitoyl glycerol (MPG) were used, either pristine or functionalised with either glucosamine or transferrin. These were first used to encapsulate Hoechst 33342 cargo to test for BBB interaction and brain penetration using *in vitro* and *in vivo* methods. NISV were then used to encapsulate a rabbit IgG-FITC to elaborate characteristics of BBB penetration *in vitro* (astrocyte cell uptake and release of IgG cargo). Finally, we demonstrate that VEEV-infected mice treated with anti-VEEV monoclonal antibody Hu1A3B-7 delivered in NISV formulations have improved survival and reduced tissue virus load.

2. Results

2.1. Generation of Glucosamine- and Transferrin-coated vesicles (gNISV and tNISV)

The NISV platform was modified through the addition of palmitoylated glucosamine (gNISV) or coating with transferrin (tNISV) to aid BBB-targeted delivery of the vesicles. Formulations were generated on the NanoAssemblr™ to include non-specific rabbit IgG (MW 150 kDa) or Hoechst 33342 in the preliminary stages and subsequently human IgG-FITC or the VEEV-specific mAb, Hu1A3B-7. The gNISV and tNISV formulations had similar antibody entrapment efficiencies of 25–30% (Fig. 1 a), typical for the entrapment of proteins using microfluidics [21]. Mean sizes were 200-390 nm and zeta potential ranged from -20 mV to -10 mV. Charged NISVs are more stable than uncharged NISV, with less aggregation and fusion [22] and this is reflected in minimal cargo leak in the absence of metabolizing cells (Fig. 1 b, 'no cells').

2.2. NISV BBB interaction and brain penetration

Initially Hoechst 33342 dye was loaded into NISV, gNISV and tNISV formulations as cargo for testing *in vitro* using the mouse BBB endothelial cell line bEND.3 and *in vivo* using the BALB/c mouse. Hoechst is a substrate for BBB efflux transporters and so normally crosses the BBB poorly [23]. However, both *in vitro* and *in vivo* data (Fig. 2) demonstrate NISVs can deliver this cargo to brain.

In vitro, NISVs were more successful at delivering Hoechst cargo to the bEnd.3 cells, compared to unencapsulated Hoechst (Fig. 2 a). In particular, gNISV delivered significantly more cargo than NISV or tNISV. In toxicity assays (Fig. 2 b), Hoechst alone reduced cell viability to 21.3 ± 0.5% of control, consistent with its DNA binding ability and perturbation of cell cycling [24]. However, toxicity was reduced after Hoechst encapsulation by NISV (Fig. 2 b), presumably because the NISV retained Hoechst and shielded the cells from toxicity. The empty NISV did not significantly change cell viability at any concentration.

In vivo, free or encapsulated Hoechst was injected i.v. into BALB/c mice, and brain and lung tissues were then removed at 2 and 4 h. Hoechst dye alone was not detected in the brain (Fig. 2 c), however, gNISV encapsulation of Hoechst resulted in increased staining in brain parenchymal cells, with the greatest signal at 2 h post-injection. By contrast, little staining was detected with unmodified NISV- or tNISV-encapsulated Hoechst dye (Fig. 2 c, left panels), even though tNISV could cross the *in vitro* BBB (8.8 ± 0.7% of NISV-Hoechst compared to 12.0 ± 1.3% of tNISV-Hoechst; $p < .01$; $n = 3$, mean ± SEM). These data suggested that gNISV were able to cross the BBB and release their cargo. All formulations successfully delivered Hoechst cargo to the lungs (Fig. 2 c, right panels), Delivery of Hoechst cargo by NISV formulations was also seen in liver and spleen tissues however no difference was seen between free Hoechst and NISV formulations (Fig. S1).

The NISVs were then used to encapsulate monoclonal antibody Hu1A3B-7 and were injected i.v. into BALB/c mice to test for the ability to deliver large therapeutics *in vivo* (Fig. 2 d). Similar to the Hoechst tests, both gNISV and tNISV increased brain delivery compared to unencapsulated Hu1A3B-7 mAb, however the gNISV formulation resulted in stronger signals at 2 h and 4 h compared to the tNISV formulation. Delivery to peripheral organs (lungs, Fig. 2 d; liver and spleen, Supplementary Fig. S2) was the same regardless of the formulation used. Evidence of antibody crossing the blood-brain barrier was confirmed by immunohistochemical staining of cargo antibody (Fig. 2 e) and demonstrated that the antibody not only associated with brain vasculature but was also present in the wider brain parenchyma.

The enhanced *in vitro* and *in vivo* delivery of gNISV cargo (Fig. 2 a, c and d) suggests glucosamine can target the BBB, and although glucosamine transporter GLUT2 is not present, glucosamine does have affinity for the enriched BBB glucose transporter, GLUT1. We tested for functional interaction between glucose uptake *versus* glucosamine or gNISV using primary porcine brain endothelial cells (PBEC) because they highly express GLUT1 and the transporter is polarized to the luminal (blood side) of the cells [25]. Glucosamine alone inhibited uptake of non-metabolized 3-O-[Methyl-D-1-3H]-Glucose with an IC50 of 4.06 ± 1.22 mM, confirming interaction (Fig. 2 f). Uptake of 3-O-[Methyl-D-1-3H]-Glucose was also reduced by gNISV at our assay concentration (0.375 mM), but not by unmodified NISV, (Fig. 2 g). These data support the proposition that gNISV interacts with GLUT1, since 1) free glucosamine inhibits cell uptake of the GLUT1 substrate glucose, and 2) gNISV (but not NISV) also inhibit GLUT1 substrate uptake. Despite the challenge to glucose uptake, there was no change in cell viability during these assays (MTT assay relative to control: NISV 102.1 ± 1.7%; gNISV 95.6 ± 2.0%; glucosamine 96.4 ± 6.1%; n = 8–18).

2.3. Characteristics of BBB penetration in vitro and cellular uptake by astrocytes

Primary porcine brain endothelial cells (PBEC) were used to examine in more detail gNISV transport across the BBB (Fig. 3 a). gNISV was labelled with $DiIC_{18}$, then loaded with FITC-labelled human IgG cargo and transport measured across the BBB monolayer from the apical (blood) side to the basal (brain) side at multiple time points

a

Formulation	Size (nm)	Zeta (-mv)	PDI	% Entrapment
NISV IgG	300	20	0.7	32
gNISV IgG	315	17	0.6	30
tNISV IgG	316	10	0.5	25
gNISV Hu1A3B-7	200	13	0.4	26
tNISV Hu1A3B-7	390	13	0.4	30

b

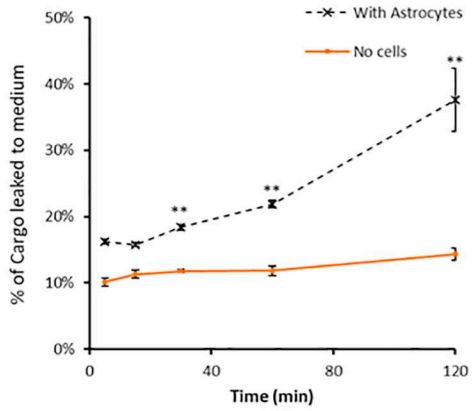

Fig. 1. NISV formulation characteristics incorporating antibodies, and cargo leak under assay conditions. (a) Values are for NISV formulations generated on the NanoAssemblrTM, modified with either transferrin or palmitoylated-glucosamine coatings (tNISV or gNISV respectively) with either rabbit IgG or Hu1A3B-7 mAb entrapment. Vesicle size and zeta potential were measured using a Malvern Zeta Sizer. Percentage antibody entrapped in NISVs was determined using Bradfords assay following removal of un-entrapped cargo. Data are the means of 3 independent samples. (b) gNISV-IgG-FITC was incubated in DMEM at 37 °C in cell culture plates (no cells) for 2 h and sampled for free IgG-FITC. For comparison, plates with primary rat astrocytes were treated in the same way. Data are expressed as percentage of initial encapsulated IgG-FITC. Values are mean ± SEM. **p < .01 *vs* 'no cells', N = 4–6.

(Fig. 3 b). By 60 min, gNISV had delivered 9 times more IgG to the basal side compared with unencapsulated IgG, with very little cargo staying inside endothelial cells (< 1%, data not shown). The BBB permeability was not changed by incubation with NISVs, as measured by FITC-Dextran 70 apical to basal transport in the presence of NISVs (FITC Dextran 70 transport was 0.40 ± 0.05% dose alone, 0.42 ± 0.08% with NISV and 0.45 ± 0.04% with gNISV; n = 6, mean ± SEM). In addition, primary astrocytes which acted as the CNS target cell (in the basal well, below the BBB monolayer), significantly accumulated cargo IgG (Fig. 3 c). Astrocyte uptake reached 3% dose by 2 h, more than 10× the uptake of unencapsulated IgG-FITC. Interestingly, astrocytes accumulated IgG cargo at an increasing rate over the course of the assay, whilst the gNISV accumulation began to plateau (Fig. 3 d), suggesting a separation of cargo and gNISV delivery vesicle in astrocytes after uptake.

Confocal microscopy visualized the $DiIC_{18}$ (red) gNISV and FITC (green) IgG transit across the BBB monolayer. Although the unencapsulated IgG-FITC was not internalized (Fig. 3 e, i. left panel), the cargo IgG-FITC encapsulated in gNISV could be clearly seen intracellularly (iii. left panel) and co-localised with gNISV-$DiIC_{18}$ (iii. right panel) confirming gNISV delivery of cargo to the cells. The gNISV was distributed throughout the cell, but in particular at junctions between cells (Fig. 3 f, arrow heads). Deformation of the cell membrane was seen in places, and some internalized gNISV was associated with plasma membrane (stained with wheat germ agglutinin, arrows Fig. 3 f), suggestive of endocytosis.

Since confocal imaging was suggestive of gNISV uptake by endocytosis at the BBB (Fig. 3 f) we tested transcellular transport at low temperature and with an endocytosis inhibitor of dynamin. In both assays, 52% of transport was inhibited, showing partial temperature dependence (Fig. 4 a) and involving a dynamin-dependent mechanism (Fig. 4 d). These data are indicative of classical endocytosis involving plasma membrane budding into a pit, closure of the opening with dynamin before pinching off and internalisation of vesicle and contents [26]. Although there was some leak of IgG-FITC cargo into the medium on the apical side of the cells (Fig. 4 b), over 95% of cargo delivered to the basal side of the monolayer was retained by the gNISV (Fig. 4 c) after 1 h, which is also consistent with transcellular vesicular mechanisms which would protect the gNISV cargo from BBB metabolizing enzymes.

It was clear from confocal imaging (Fig. 4 e) that during dynamin inhibition gNISV were retained by the PBEC monolayer, rather than being transported across the cells. A possible explanation is that gNISV are trapped in mature endocytic vesicles at the cell membrane that could not pinch off and be internalized for transcytosis. Since dynamin is a key protein involved in endocytosis, further immunocytochemistry was carried out to determine whether the gNISV associated with clathrin (classical receptor-mediated endocytosis), or EEA1 (marker of early endosomes and sorting endosomes) or 58 K-9 (marker of Golgi filaments and trafficking between the ER and the Golgi) and all proved negative (Supplementary Fig. S3).

To further understand the mechanisms for accumulation of gNISV and the IgG cargo by astrocytes, low temperature transport conditions and studies using inhibitors of endocytosis were carried out using similar approaches as used to determine PBEC monolayer transport. At 4 °C, astrocyte uptake of $DiIC_{18}$-labelled gNISV and the FITC-labelled IgG cargo was reduced by 70% and 93% respectively (Fig. 5 a) implying an energy dependent mechanism. This is a greater impact than similar conditions had on PBEC transport of gNISV, as described above. Dynamin inhibition resulted in an accumulation of gNISV at the cell membrane (Fig. 5 b) in astrocytes, as was seen in the studies using PBECs. Confocal imaging also showed that astrocyte uptake of gNISV and IgG cargo was associated with both clathrin and peri-nuclear EEA1, a marker of sorting endosomes (Fig. 5 c). This is a typical pathway for receptor-mediated endocytosis [27]. There was also intracellular trafficking of labelled IgG cargo through the ER-Golgi which was inhibited by the addition of Brefeldin A (Fig. 5 d) and cargo accumulates in the peri-nuclear space when trafficking is inhibited (Fig. 5 e).

2.4. In vivo assessment of gNISV to treat Venezuelan equine encephalitis virus infection

Following successful transfer of cargo by gNISV across the BBB to target CNS cells, we then tested the ability of gNISV encapsulated Hu1A3B-7 to treat VEEV infection in mice. Formulations were tested in neutralisation assays to ensure the VEEV-specific mAb maintained antiviral activity. The activity of this batch of Hu1A3B-7 was low to help to clarify the impact of formulation on efficacy (stock antibody had 50 μg/ml specific reactivity to VEEV), but the process of encapsulation and freeze drying had no detrimental effect on the neutralising activity of

a

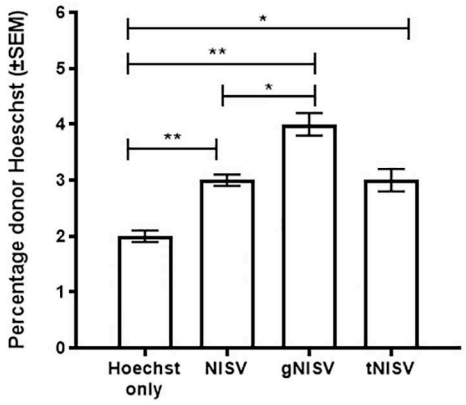

b

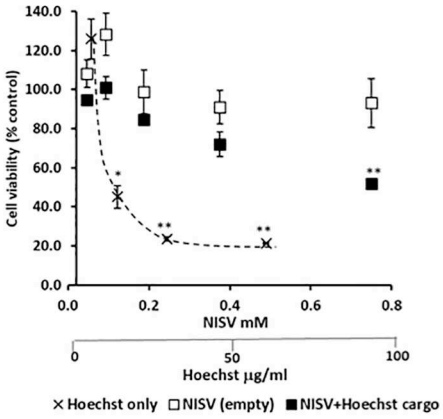

c

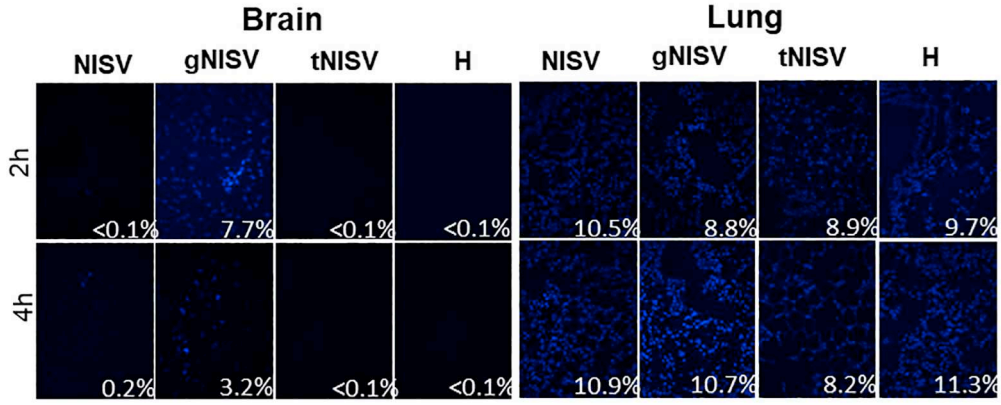

d

Brain	Hu1A3B-7 mAb	gNISV mAb	tNISV mAb
2h	1.03 ± 0.223	2.318 ± 0.729	1.436 ± 0.302
4h	1.148 ± 0.219	4.672 ± 0.134	2.198 ± 0.587
24h	0.18 ± 0.147	0.862 ± 0.177	0.814 ± 0.2737
Lung	**Hu1A3B-7 mAb**	**gNISV mAb**	**tNISV mAb**
2h	2.312 ± 0.237	2.288 ± 0.43	2.456 ± 0.567
4h	2.302 ± 0.508	2.598 ± 0.394	2.678 ± 0.559
24h	1.026 ± 0.112	0.656 ± 0.405	0.636 ± 0.344

e

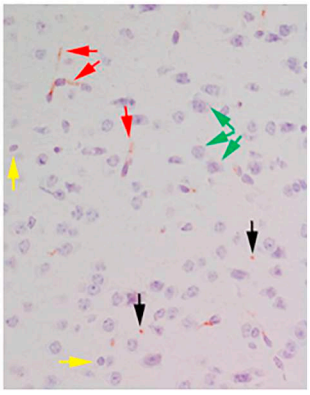

f

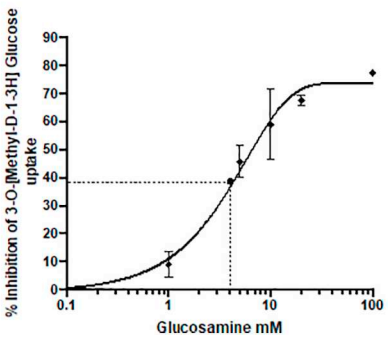

g

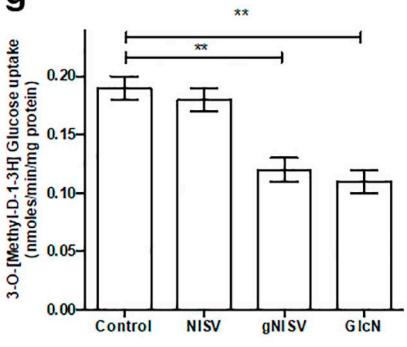

(caption on next page)

Fig. 2. gNISV is better than tNISV at delivering cargo to the brain: Hoechst dye and monoclonal antibody Hu1A3B-7 mAb delivery. (a) gNISV delivers cargo to BBB cells *in vitro*. Brain endothelial cell line bEND.3 uptake of Hoechst 33342 over 1 h, added alone or encapsulated in NISV formulations. Hoechst uptake was greatest when encapsulated in gNISV, compared to the other formulations (*p < .05) or unencapsulated Hoechst (**p < .01). Hoechst concentration was 10 μg/ml added either free or encapsulated in 0.05 mM NISV formulations, mean ± SEM N = 4. (b) *In vitro* BBB cell viability with free Hoechst, empty NISV and NISV with Hoechst cargo. The NISV protects bEND.3 endothelial cells from Hoechst toxicity, assessed by MTT assay, mean ± SEM, *p < .05, **p < .01, N = 3. (c) gNISV delivers cargo to brain *in vivo*. NISV formulations loaded with Hoechst dye, or Hoechst alone (H) were injected i.v. into BALB/c mice. After 2 h or 4 h, brain and lung tissue were removed and slices examined for Hoechst staining (blue) and quantified by measuring the percentage area of an image positive for the Hoechst stain. (d) gNISV delivers monoclonal antibody Hu1A3B-7 to the brain *in vivo*. NISV formulations loaded with Hu1A3B-7 mAb were injected i.v. into BALB/c mice. At 2 h, 4 h and 24 h post injection, brain and non-CNS (lung) tissues were removed and stained for Hu1A3B-7 mAb and quantified as percentage area of the image positive for staining. (e) Representative image of Hu1A3B-7 mAb staining in BALB/c mouse brain after delivery with gNISV. Immunohistochemical detection of the antibody: Red arrows, positive staining within the lumen of brain capillaries; Black arrow heads, positive staining within the neuropil (extravascular); Green arrows, neuronal nuclei; Yellow arrows, glial cell nuclei. (f) and (g) gNISV interacts with BBB glucose transport in primary porcine brain endothelial cells (PBEC). Uptake of trace 3-O-[Methyl-D-1-3H]-Glucose was inhibited by free glucosamine with an IC50 of 4.064 ± 1.221 mM (df = 17) and Hill coeff. -1.524 ± 0.638 (http://www.ic50.tk/). Uptake of 3-O-[Methyl-D-1-3H]-Glucose by porcine brain endothelial cells was inhibited by gNISV. Cells remained untreated or were treated with 0.375 mM NISV, 0.375 mM gNISV or 5 mM glucosamine (GlcN). N = 4–7, **p < .01 compared to control. (For interpretation of the references to colour in this figure legend, the reader is referred to the web version of this article.)

the mAb.

BALB/c mice were exposed to approximately 150 × 50% lethal doses (LD50) of VEEV TrD strain by the aerosol route (approximately 25pfu retained dose). Clinical signs of infection appeared at approximately 2 days post-infection (p.i.) with time to death typically between 5 and 6 days. The treatment model was one intraperitoneal injection at 24 h p.i., which has previously been shown to be consistent and suitable for assessing the efficacy of Hu1A3B-7 [3].

Both the NISV Hu1A3B-7 and gNISV Hu1A3B-7 formulations performed significantly better than unencapsulated Hu1A3B-7, with around 50% mice still alive at 20 days p.i. (p = .0294, p = .0030 respectively). (Fig. 6 a). Of interest to this study, the only treatment that significantly reduced viral titre in the brain was gNISV Hu1A3B-7 (Fig. 6 b), compared with both controls, with a reduction of 3–4 logs.

Encapsulation of Hu1A3B-7 reduced viral titre in peripheral tissues including the lung, liver and spleen (Fig. 6 c, d, e). In the lung and liver, reduced viral titres were seen when the mAb was delivered with either NISV or gNISV, but not with unencapsulated Hu1A3B-7. Importantly, the spleen data also showed that unencapsulated Hu1A3B-7 still provided therapeutic benefit (Fig. 6 e).

3. Discussion

Treatment of CNS and brain diseases is a growing area of research and concern, but is difficult due to the highly complex BBB that has evolved to selectively limit and tightly regulate entry and passage of compounds and molecules into the CNS [28]. The BBB also contains efflux transporters such as p-glycoprotein and is responsible for active efflux of various molecules limiting their ability to reach or maintain therapeutic exposure levels. Indeed, it has been stated that approximately 98% of small molecule drugs and almost 100% of large molecule drugs are blocked from entering the brain [29]. This presents a barrier for drug development and means that some therapies struggle to have an impact *in vivo* despite early promise *in vitro* [30].

Several therapeutic strategies have been employed to facilitate the passage of drugs across the BBB including co-administration of agents that cause non-selective temporary opening of the BBB (for example by ‘osmotic shock’ or focused ultrasound or use of specific efflux transport inhibitors such as Tariquidar, a specific p-GP inhibitor) [31,32]. However, these invasive techniques are non-selective and of limited value. A well-studied strategy is to utilise nanoparticles to transfer the cargo across the BBB. Many of these delivery platforms have been coated to aid targeted tissue delivery. For receptor-mediated transcytosis into the brain [33], several commonly and preferentially expressed receptors in brain tissue have been targeted and include the transferrin receptor, insulin receptor, and lipoprotein receptor-related protein [34–36]. For small molecule drugs, transport using the glucose transporters (GLUTs) have been explored. GLUT1 is greatly enriched at the BBB because the brain relies on glucose as its main source of energy. The GLUT1 facilitated diffusion solute transporter delivers glucose to the brain at a rate ten-times higher than other tissues, making the brain the main consumer of glucose in the body [11]. Thus GLUT1 is an attractive target for brain delivery. Transferrin has also been shown to facilitate delivery of directly conjugated drugs or nanoparticle-associated drugs across the BBB. In the studies described herein, we chose to compare both transferrin and GLUT1, as each transports molecules across the BBB using distinct mechanisms and both have shown promise in several different disease models, including brain tumors [34].

All NISV formulations were able to encapsulate antibody, which at approximately 150 kDa is a large biological compound, and all formulations delivering antibody cargo performed better in terms of traversing the BBB than non-entrapped cargo. Interestingly, in our *in vitro* and non-infectious *in vivo* studies, the gNISV consistently outperformed transferrin-coated NISV. Consequently, gNISV were taken forward for further studies of *in vitro* BBB transport and testing of entrapping and delivering therapeutic Hu1A3B-7 in the VEEV infection model. The relatively modest improvement in cargo delivery using transferrin-coated vesicles was somewhat surprising. Previous studies targeting the transferrin receptor-mediated transport of antibodies, have shown high affinity binding to the transferrin receptor prevents transcytosis and can deliver the antibody to lysosomes [37]. Since alternative transferrin formulations have shown promise *in vivo*, modifications to transferrin concentration and coating methods may yet be useful for NISV platforms in the future.

Using an *in vitro* model of the BBB we dissected the complex mechanism for gNISV transport across the BBB. The process is partially energy dependent and involves both dynamin-dependent and independent mechanisms. Around half of transport was dynamin-dependent, indicative of classical endocytosis involving plasma membrane budding into a pit, closure of the opening with dynamin before pinching off and internalisation of vesicle and contents [26]. Since the gNISV did not co-localise with clathrin, transport is unlikely to involve receptor-mediated endocytosis, but could be caveolae-mediated [38]. In addition, gNISV did not co-localise with EEA1, a marker of early endosomes and peri-nuclear (Golgi-associated) sorting/late endosomes [38]. Since the sorting/late endosomes are acidified compartments [39], the gNISV would degrade if localised there. Therefore, the lack of EEA1 association is consistent with the intact transport of gNISV across the BBB observed (Fig. 4 c). Just under half of BBB gNISV transport was dynamin-independent which is not well described in BBB endothelial cells [40]. Dynamin- and clathrin-independent endocytosis tends to involve high capacity larger volume (0.1–1 μm) vesicles [38] and includes the CLIC (clathrin-independent carriers) systems of tubular vesicles which develop from the plasma membrane; our NISVs are within this size range (0.2–0.4 μm). CLICs are known to endocytose a wide range of cell surface proteins including GLUT1, and to recycle plasma membrane [38]. In our study of gNISV, the plasma membrane deformation observed in the presence of gNISV combined with evidence for dynamin-

independent endocytosis is consistent with CLIC-mediated endocytic pathways. We hypothesise that glucosamine decoration of NISV may increase its 'dwell time' at the BBB due to interaction with GLUT1, and this increases the likelihood of CLIC pathway endocytosis of the GLUT1 and plasma membrane along with the gNISV. This is more plausible than gNISV being directly transported by the GLUT1 solute transporter, which typically mediates facilitated diffusion of the small hydrophilic saccharides, glucose, galactose and mannose [41]. In support of our

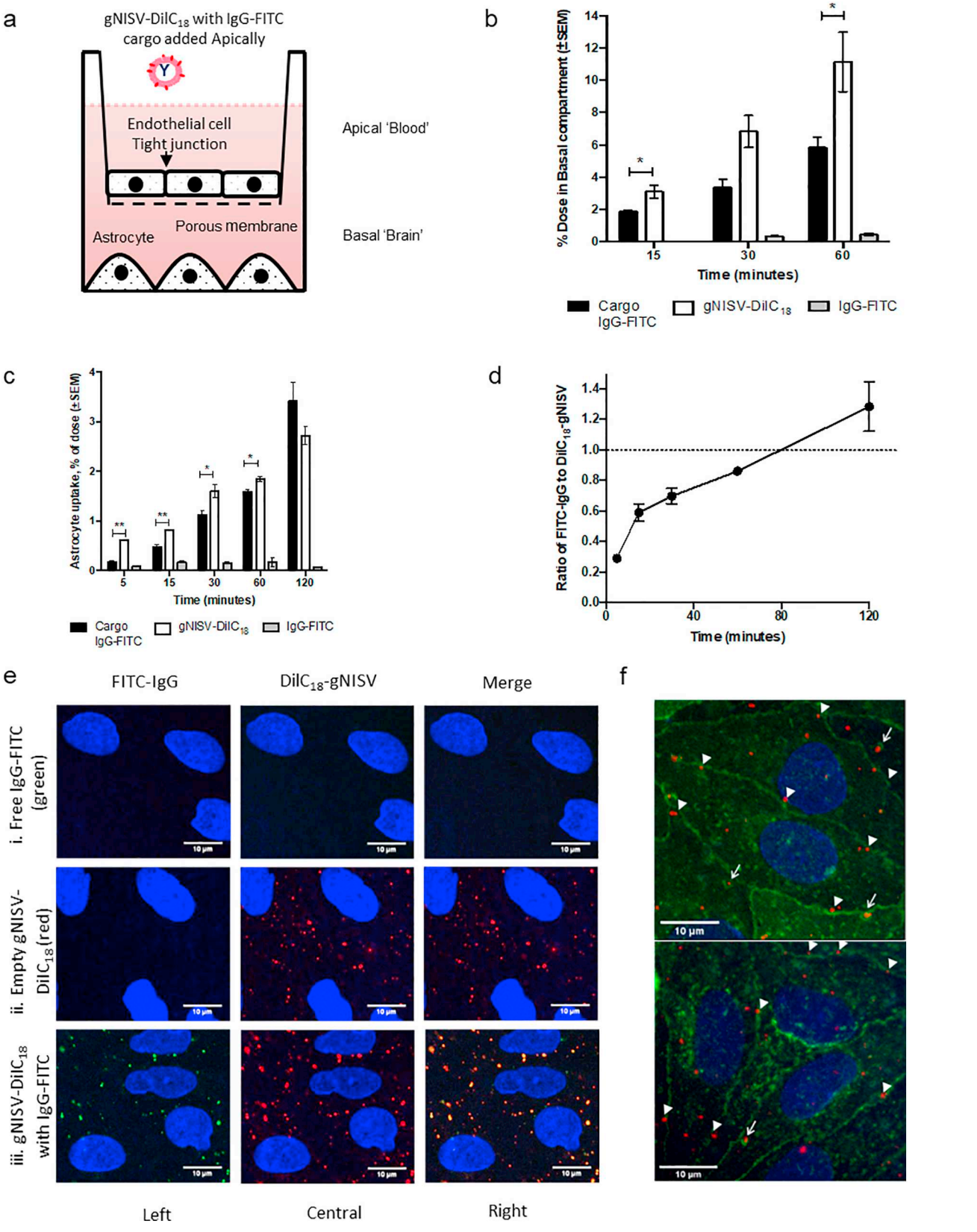

(caption on next page)

Fig. 3. gNISV formulations loaded with IgG cargo are transported across the *in vitro* BBB and taken up by astrocytes. (a) Primary porcine brain endothelial cells (PBECs) were grown on permeable Transwell filters above primary rat astrocytes (non-contact co-culture). IgG-FITC cargo entrapped in $DilC_{18}$ labelled gNISV was added to the apical (Blood side) compartment. Samples were taken from the basal (Brain side) compartment at different time points and assayed for IgG-FITC and for gNISV-$DiIC_{18}$. (b) BBB apical to basal transport of 0.375 mM gNISV-$DiIC_{18}$ and its cargo IgG-FITC, expressed as % of apical formulation appearing in the basal compartment, % dose. As a control, apical to basal transport of free (un-encapsulated) IgG-FITC was assessed in separate cells. *p < .05 difference between gNISV and IgG cargo, N = 4–6. (c) Astrocyte uptake of gNISV-$DiIC_{18}$ and its IgG-FITC cargo, expressed as % dose. Uptake of free (un-encapsulated) IgG-FITC assessed as a control in separate cells. *p < .05, **p < .01, difference between gNISV and IgG cargo, N = 3. (d) Astrocyte uptake shows increased accumulation of IgG cargo (FITC) relative to the gNISV ($DiIC_{18}$). N = 3 (e) PBECs incubated for 30 min with: i. IgG-FITC alone, ii. empty gNISV-$DiIC_{18}$, iii. gNISV-$DiIC_{18}$ with IgG-FITC cargo. Confocal microscopy magnification x40. (f) PBECs incubated with empty gNISV-$DiIC_{18}$ (red) and plasma membrane stain WGA-488 (green). Magnification x100. (For interpretation of the references to colour in this figure legend, the reader is referred to the web version of this article.)

hypothesis, Machut-Binkowski et al. [42] noted that coating liposomes (150 nm) with glucose enhanced BBB uptake compared with non-coated liposomes in bovine BBB endothelial cells. This proposal of a clathrin-independent endocytosis pathway, involving increased 'dwell time' of a nanoparticle at the BBB through interaction with a membrane protein, is a novel approach for NISV and antibody brain drug delivery and broadens BBB targeting strategies.

In astrocytes, uptake of the gNISV follows a more traditional mechanism of dynamin-dependent, clathrin-mediated endocytosis with the cargo observed in EEA1-marked peri-nuclear sorting endosomes. The gNISV carrier appears to be separated from the IgG cargo during this process, and the cargo is trafficked from the Golgi to endoplasmic reticulum for further processing. The different mechanisms we observed for gNISV endocytosis between the BBB (transcellular transport) and astrocytes (cellular accumulation, separation of gNISV and cargo and intracellular IgG cargo trafficking to Golgi/ER processing) provide explanatory mechanisms for how gNISV are able to effectively deliver therapeutic molecules to the brain *in vivo* (Fig. 2 c, d, e, f). This would suggest that the gNISVs specifically designed to deliver cargo to the brain are capable of targeting this tissue and delivering therapeutically relevant concentrations of cargo.

To examine the advantages of encapsulating therapies in to NISV platforms we used an *in vivo* VEEV infection model with the Hu1A3B-7 therapeutic antibody entrapped in the vesicles. Previous studies have

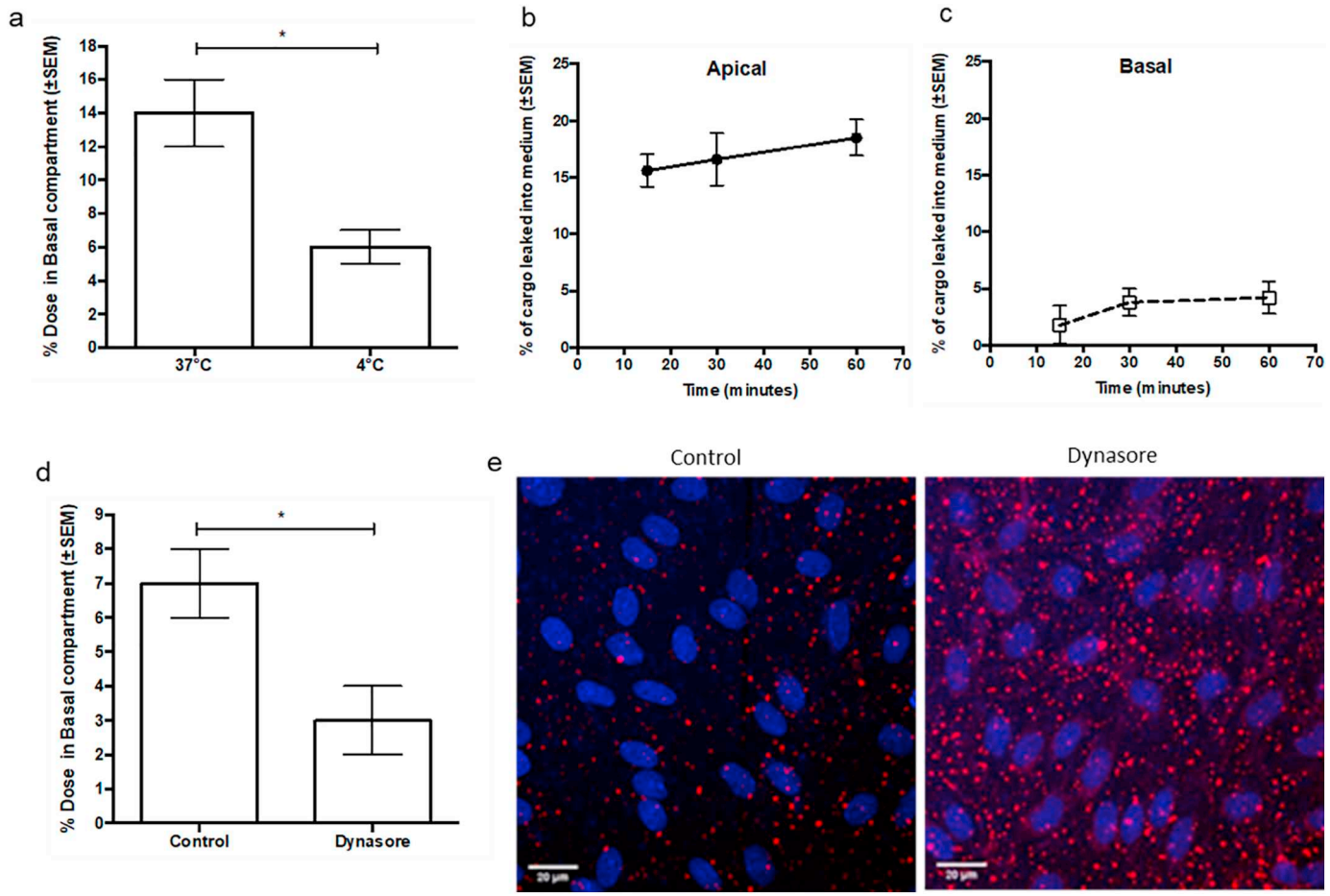

Fig. 4. gNISV-$DiIC_{18}$ transport across PBEC monolayers on Transwell filters. Effect of low temperature and inhibition of dynamin endocytosis. (a) After 60 min at 37 °C or at 4 °C; *p < .05 difference between 37 °C and 4 °C (b) and (c) IgG-FITC cargo 'leak' from gNISV during transport across the PBEC. IgG-FITC loaded gNISV-$DiIC_{18}$ formulations were added to the apical compartment and samples taken from (b) apical and (c) basal compartments after,15, 30 and 60 min incubation. Released 'leak' IgG-FITC cargo measured. Values are mean ± SEM. N = 4–6 (d) Cells were pre-incubated for 30 min with dynamin-dependent endocytosis inhibitor, dynasore, or vehicle control, then 0.375 mM gNISV added for a further for 30 min. *p < .05 difference to control, N = 3–6. Dynasore treatment did not change functional permeability of the monolayers, as measured by free FITC-IgG permeability (Papp; control 0.72 ± 0.12, dynasore 0.58 ± 0.12 × 10^{-6} cm.sec^{-1}; n = 3–4, p > .05, mean ± SEM). (e) Imaging of red gNISV-$DiIC_{18}$ retained by the PBEC cell monolayer (x20 magnification) in control and dynasore-treated cells. (For interpretation of the references to colour in this figure legend, the reader is referred to the web version of this article.)

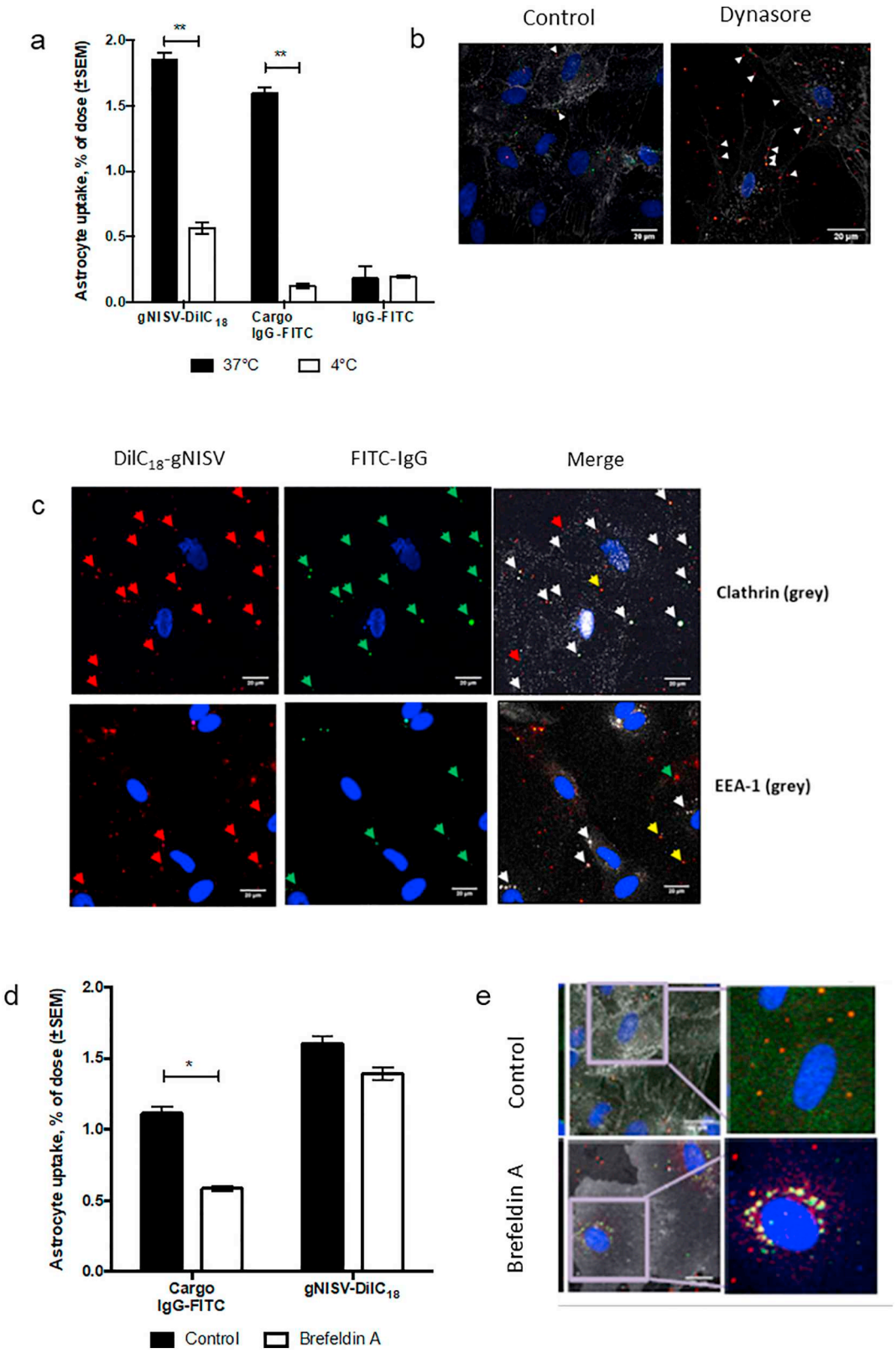

Fig. 5. gNISV-DiIC$_{18}$ and IgG-FITC cargo uptake by Astrocytes: Effect of low temperature, dynamin inhibition, co-localisation with endocytosis proteins, and intracellular trafficking inhibition. (a) Low temperature, 4 °C, reduces astrocyte accumulation of gNISV-DiIC$_{18}$ and IgG-FITC cargo, but not of free (un-encapsulated) IgG-FITC. Incubations were 60 min. **p < .01 difference between 37 °C and 4 °C, n = 3. (b) Accumulation of gNISV-DiIC$_{18}$ at astrocyte cell membranes after 30 min with dynamin inhibitor, dynasore (x40 magnification). (c) Co-localisation of gNISV-DiIC$_{18}$ (red arrow heads) with cargo IgG-FITC (green arrow heads) and clathrin staining (grey arrow heads) in the upper panels or peri-nuclear EEA-1 staining (grey arrow heads) lower panels (x40 magnification). (d) Inhibition of endoplasmic reticulum-Golgi trafficking using Brefeldin A results in reduced accumulation of IgG-FITC cargo but no change in gNISV-DiIC$_{18}$ uptake. Incubations were 30 min, *p < .05, **p < .01 difference compared to control, n = 4–5. (e) Astrocyte perinuclear accumulation of IgG-FITC cargo after inhibition of ER-Golgi trafficking using Brefeldin A (x40 magnification). (For interpretation of the references to colour in this figure legend, the reader is referred to the web version of this article.)

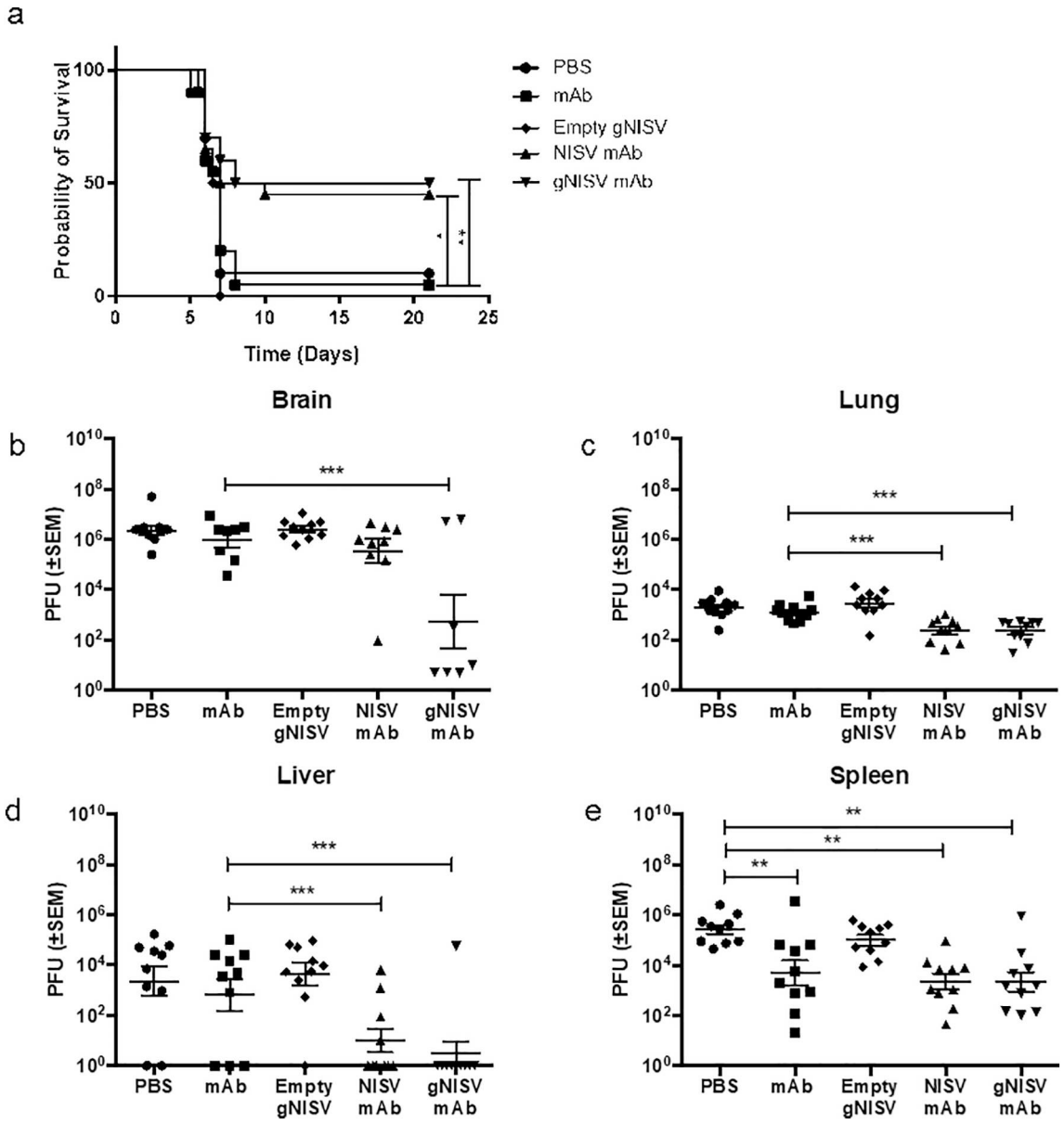

Fig. 6. Encapsulated Hu1A3B-7 VEEV mAb formulations enhanced survival compared to free Hu1A3B-7 VEEV mAb in an aerosol model of VEEV. (a) Kaplan Meier plot of BALB/c mice challenged with aerosolised VEEV, with 20 mice per group, from 2 independent experiments. PBS and empty gNISV treatment groups were included as controls. Either NISV mAb, gNISV mAb or mAb alone were given to each treatment group. A total of 10 mice per treatment group (5 per independent experiment) were culled at d5 p.i. with viral titre determined in the brain (b) lung (c), liver (d), spleen (e). *P < .05, **p < .01, ***p < .001 ANOVA multiple comparisons.

shown that Hu1A3B-7 is efficacious in protecting mice against VEEV, when given as a single dose at 24 h and 48 h p.i. [3]. In our studies we used a sub-optimal dose of Hu1A3B-7 which helped to clarify the impact of formulation on efficacy. In this murine infection model, both the uncoated NISV and the gNISV significantly reduced viral titres in the lung and liver which was not observed with unencapsulated mAb. Importantly gNISV carrying Hu1A3B-7 was the only formulation to significantly reduce VEEV titres in the brain relative to that seen in control non-treated animals. Despite the obvious difference in brain viral load, the gNISV and NISV performed equally well in their ability to promote survival. This is somewhat surprising since the presence of virus in the brain is thought to be a key contributor to VEEV-induced morbidity and mortality [18,19]. Interestingly, a recent paper using the TC-83 strain of VEEV, demonstrated that therapeutic ML-336 in lipid coated mesoporous silica nanoparticles could reduce VEEV load in the brain, but only by one half a log, and this did not correlate with increased survival at the concentrations tested [43]. In our study presented here, viral load decreased by 3–4 logs in brain tissue of mice infected with the TrD strain of VEEV, which may explain the difference between our studies. Overall however, improvements in the peripheral tissues demonstrate the ability of both NISVs to increase efficacy of sub-optimal levels of therapeutic compound, while the gNISV encapsulated mAb showed additional benefits in the brain.

In summary, data generated in these studies highlights the huge potential of glucosamine-decorated NISV as a drug delivery platform. NISVs are easier to manufacture than liposomes, can entrap a wide range of drugs and are easier to handle in terms of sterilization and stability. We show that the NISV platform can entrap large complex compounds (biologics) such as IgG and can be coated for targeted brain delivery. Further, the ability to transfer a large protein complex cargo across the BBB without degradation, to deliver it to target CNS cells and for the mAb to retain antiviral efficacy is greatly encouraging. The

potential applications for the gNISV formulations could be broadened, for example to entrap anti-cancer or anti-malarial drugs to combat diseases of wider public health concern.

4. Materials and methods

4.1. N-palmitoyl glucosamine (NPG) synthesis

All reagents were sourced from Sigma Aldrich, UK. NPG was produced using a previously described method [12] with some modifications. Briefly, glucosamine (86.3 mg) was dissolved in 15 ml of dimethyl sulphoxide with 93 μl of triethanolamine. Palmitic acid N-hydroxysuccinimide (283 mg) was dissolved in 4 ml of chloroform. Once both solutions had completely dissolved, they were mixed and stirred for 48 h at room temperature, in the dark. The palmitoylated-glucosamine was precipitated out by chilling the mix and adding ice-cold water. The mix was then applied to a vacuum filter to separate the precipitate. Separate water, chloroform and ethanol washes were applied to the palmitoylated-glucosamine before drying at 40 °C for 48 h.

4.2. Human holo-transferrin thiolation

Human holo-transferrin (Sigma Aldrich, UK), previously shown to interact with murine transferrin receptors [15,34], was modified with a thiol by mixing transferrin with a 10-fold molar excess of Traut's reagent (Sigma Aldrich, UK) at 25 °C for 1 h. Excess Traut's reagent was removed using a Vivaspin 6 column (Sartorius) with a 5 kDa molecular weight cut-off.

4.3. Vesicle preparation using microfluidics

Vesicles were prepared using the NanoAssemblrTM benchtop (Precision Nanosystems) with a 300 μm staggered herringbone micromixer chip held at a temperature of 60 °C. The vesicle components (mono-palmitoyl glycerol, cholesterol and dicetyl-phosphate, all Sigma-Aldrich, UK) were solubilized in methanol at a 5:4:1 ratio with a total concentration of 5.62 mg/ml and heated to 60 °C. Antibodies (either Rabbit IgG (Sigma Aldrich, UK), Hu1A3B-7 or Human IgG-FITC (Sigma Aldrich, UK)) were solubilized in PBS at 2 mg/ml. The aqueous and solvent streams were mixed at a ratio of 3:1, with a combined flow rate of 12 ml/min. Drug encapsulation and vesicle formulation occurs simultaneously within the microfluidic chip. The methanol and unentrapped drug were removed using a Vivaspin 20 column (Sartorius) with a 300 kDa molecular weight cut-off. Concentration of entrapped antibody was determined using a standard Bradford's protein assay. gNISV were prepared in the same manner but with the addition of 6.4 mg palmitoylated glucosamine to the vesicle components dissolved in methanol. tNISV were synthesized by including PEG-Maleimide (Tebu-Bio) in the NISV mix. Following removal of the methanol and unentrapped cargo the vesicles were incubated with the thiolated transferrin for 1 h at 25 °C. Excess transferrin was then removed using a Vivaspin 20 column with a 100 kDa molecular weight cut-off.

4.4. Preparation of fluorescent NISV formulations

Fluorescent NISV formulations were generated through the entrapment of Hoechst 33342 (Sartorius) to stain cells which interact with the NISV or through the incorporation of $DiIC_{18}$ (Life Technologies) into the NISV membrane structure. For Hoechst-loaded NISV formulations, 3 mg/ml Hoechst 33342 in PBS was loaded into the aqueous side of the NanoAssemblr™. A Hoechst standard curve was prepared to quantify entrapped Hoechst. For the directly labelled NISV formulations, 0.2 mol of $DiIC_{18}$ was mixed with the surfactant components dissolved in methanol. Vesicle synthesis for both variations was then carried out on the NanoAssemblrTM as described. NISV formulations were stored at −20 °C as stock 9.37 mM suspensions. Prior to use, they were defrosted, centrifuged at 14000*g* for 5 min and the supernatant aspirated to remove any leaked cargo, which was 0.43 ± 0.05% for NISV; 0.14 ± 0.03% for gNISV (SEM, n = 8), equivalent to 0.19 μg/ml and 0.08 μg/ml respectively.

4.5. Freeze drying of vesicle formulations

To facilitate transport of vesicle formulations between sites for *in vivo* studies, vesicle batches containing antibody were lyophilized. Sucrose was added to NISV preparations to a concentration of 100 mM. Preparations were placed at −80 °C for 24 h prior to being lyophilized in a Christ Epsilon 2-4LD Freeze Dryer and dried at −40 °C for 48 h with a condenser temperature of −70 °C. Following rehydration with distilled water, antibody activity was verified by neutralisation assays [2].

4.6. Characterization of NISV formulations

Vesicle size and zeta-potentials were determined using a Malvern Zeta-sizer (Zetasizer 30000HS, Malvern Instruments Ltd., UK).

4.7. In vivo assessment of Hoechst and IgG delivery

All animal procedures conformed to guidelines from The Home Office of the UK Government under the Animals [Scientific Procedures] Act 1986. All work was covered by Licence PE9F3466E,“Improving the Pharmacokinetics and Tissue Targeting of Antimicrobials” with approval by the University of Strathclyde ethical review board. BALB/c mice were bred in house at the Strathclyde Institute of Pharmacy and Biomedical Sciences, Glasgow, UK under specific pathogen free conditions. Mice were housed in polypropylene cages (13cm × 35cm), containing Ecopure flakes and sizzle nest bedding (SDS Services) with access to water and CRM mouse chow (SDS Services) *ad libatim*. Six- to eight-week-old, male BALB/c mice (University of Strathclyde) were housed in groups of 5. Mice were dosed intravenously with free cargo or NISV formulations containing either Hoechst (500 μg/per mouse) or Rabbit IgG (100 μg/per mouse). At 2, 4 and 24 h post injection, animals were sacrificed and brain, lung, liver and spleen tissues were collected. For studies using Hoechst, tissue samples were placed into 10% formalin for 3 h and subsequently transferred to 30% dextrose solution overnight. Samples were then placed into molds containing Tissue-Tek OCT resin (Somagen, Torrance, CA) and flash frozen in liquid nitrogen. For mice dosed with IgG, tissues were removed and stored in 10% formalin. Samples were shipped to the Veterinary Pathology Centre (University of Surrey) for histopathological analysis.

4.8. Immunohistochemistry

Formalin-fixed paraffin-embedded (FFPE) tissue samples were used to standardise a protocol to localise the rabbit IgG in the tissue. Tissue sections were deparaffinised and rehydrated using xylene and a graded series of ethanol and water, finishing with tris-buffered saline (TBS). Antigen re-expression was achieved through enzymatic digestion with proteinase K. The enzymatic digestion was stopped (3 washes in TBS) and followed by incubation with a 1:100 dilution of polyclonal goat anti-rabbit IgG Alexa568 labelled antibody (Invitrogen) for 30 min at room temperature. After 3 TBS washes, slides were mounted using Vectashield antifade hardset mounting media (Vector laboratories) and studied under fluorescent light in a Nikon Ni-SE microscope. Similarly, tissue sections were used for immunohistochemical detection of rabbit IgG with light microscopy, using the same antigen retrieval method. A 1:200 dilution of polyclonal biotinylated goat anti-rabbit IgG antibody (Pierce) was incubated with the tissue sections for 30 min at room temperature followed by the avidin-biotin peroxidase complex reaction (Pierce). The reaction was developed using NOVARED (Vector). Sections were counterstained with Haematoxilin and glial and neuronal

cells were distinguished by morphology.

4.9. VEEV-specific mAb and viral assays

Stocks of Hu1A3B-7 were produced as described [2] (2). ELISA and neutralisation assays were performed as previously described [2,3]. The amount of virus present within mouse tissues was determined by plaque formation under a 1.5% (w/v) carboxymethyl cellulose overlay in Vero cells (European Collection of Animal Cell Cultures). Tissues were removed and homogenized in 2 ml PBS by passing through a 70 μm nylon cell strainer (BD Falcon). Serial dilutions of the cell suspensions were added to wells of confluent Vero cells. After an incubation of 30 min at room temperature, the carboxymethyl cellulose overlay diluted in double-strength Leibovitz L-15 media was added. Cells were incubated for 72 h, fixed with 10% (v/v) formaldehyde in PBS overnight, and then stained with 0.1% (w/v) crystal violet. The plaques were counted and the amount of virus was calculated.

4.10. Animal infection studies

All animal infection studies confromed to guidelines from The Home Office of the UK Government under the Animals [Scientific Procedures] Act 1986 and carried out under licence P1D46FB69. Stocks of VEEV Trinidad Donkey (TrD) were prepared as described [2,3]. Six- to eight-week-old female BALB/c mice (Charles River, UK) were transferred to a high-containment class III rigid isolator, where they were assigned randomly to groups and given unlimited access to food and water. Mice were challenged with approximately 150 × 50% lethal doses (LD50) VEEV TrD *via* the aerosol route, using a Biaera aerosol management platform, as described previously [3]. This equates to approximately 25pfu retained dose per animal [44]. Mice were observed twice daily and scored for clinical signs. Twenty-four hours after the viral challenge, various treatments (PBS, Hu1A3B-7, empty gNISV, NISV Hu1A3B-7, gNISV Hu1A3B-7) were administered by the intraperitoneal route. Mice received 100 μg of Hu1A3B-7 based on the total protein concentration (10% VEEV specific activity, determined by ELISA) of the stock antibody solution. Mice were euthanized five days post-challenge for analysis of tissues or at pre-determined humane endpoints. All procedures and housing were in accordance with the United Kingdom Animal (Scientific Procedures) Act (1986).

4.11. Cell viability MTT assay

bEnd.3 endothelial cells were seeded into fibronectin coated 96 well plates at 10,000 cells per 0.33cm^2 well in 200 μl ATCC medium, 10% FCS and grown until confluent. Increasing concentrations of NISV formulations (0.047–1.5 mM) with or without a Hoechst cargo, or unencapsulated Hoechst 33342 (7-250 μg/ml) were added and cells incubated for 1 h on an orbital shaker at 100 rpm at 37 °C. Cells were either washed with assay buffer and fluorescent Hoechst signal read (Bio-Tek Synergy HT plate reader, 460/40 nm bound spectra emission, 528/20 nm unbound spectra emission), or the MTT tetrazolium dye assay was used to estimate cell viability. MTT (1 mg/ml) was added to cells, then incubated for 4 h at 37 °C, followed by propran-2-ol treatment to dissolve the formazan salt before reading absorbance with a UV plate reader at 540 nm. Results are expressed as absorbance relative to control cells, unexposed to NISV or Hoechst 33342.

4.12. Glucose uptake

To explore whether glucosamine decorated NISV interact with BBB glucose uptake transporters, 3-O-[Methyl-D-1-3H]-Glucose uptake by PBEC endothelial cells was challenged with either NISV (0.375 mM), gNISV (0.375 mM) or unencapsulated D-(+)- glucosamine hydrochloride (5 mM). Confluent PBEC cells in 96-well plates (cultured as above) were pre-incubated for 20 min at 37 °C in glucose-free assay buffer (135 mM NaCl, 25 mM HEPES, 5.4 mM KCl, 1.5 mM CaCl2, 1.2 mM MgCl2, 100 mM pyruvate and 0.5% BSA, at pH 7.4). NISV or glucosamine were applied in fresh glucose-free buffer for a further 10 min, before adding trace levels of 3-O-[Methyl-D-1-3H]-Glucose (specific activity 2.96 MBq/nmole, Perkin Elmer), to a final concentration of 55KBq/200 μl/well (94 nM glucose) for 30 min. Uptake was halted with ice-cold Hanks Balanced Salt Solution (HBSS) stop solution (100 μM HgCl2 and 50 μM phloretin at pH 7.4), cells lysed with 1% Triton-x 100 for 45 min, and radioactivity determined using a 1219 Rackbeta liquid scintillation counter (LKB Wallac) in 3.5 ml of liquid scintillation cocktail (Ultima Gold, PerkinElmer). Cell lysate protein content was measured using the Pierce BCA assay kit (Thermofisher) and cell uptake of 3-O-[Methyl-D-1-3H]-Glucose is expressed as nmol/min/mg protein.

4.13. Blood brain barrier cell culture

Porcine brain endothelial cells (PBEC, BBB cells) were isolated and cultured as previously published [45]. Cells were seeded onto collagen and fibronectin coated polycarbonate Transwell filters (Corning, 1.12cm^2 filter surface area, 0.4 μm pore size), at 10 × 10^4 cells per filter in 12 well plates, and grown above Poly-L-Lysine-coated wells containing confluent primary rat astrocytes. BBB cells were grown for 3 days, then transferred to serum-free media with hydrocortisone, 8-CPT-cAMP and phosphodiesterase inhibitor RO 20-1724 for a further 2–3 days until cells formed a confluent monolayer. Routine measurements were made of monolayer tightness using two measures to confirm functionally tight monolayers: i) transendothelial electrical resistance (TEER) using a STX100C Electrode Probe with an EVOM Epithelial Voltohmmeter demonstrated high resistance, average 908 ± 66 Ωcm^2 (n = 51); ii) one-hour permeability Papp of macromolecules across the BBB monolayer demonstrated low paracellular permeability. FITC Dextran 70 kDa Papp averaged 0.6 ± 0.1 × 10^{-6} cm/s (n = 36), and IgG-FITC Papp (human, 150 kDa) was 0.56 ± 0.09 × 10^{-6} cm/s (n = 4).

4.14. BBB Transport and cell uptake assays

On the day of the assay, cell medium was replaced by a clear assay buffer of HBSS, 0.5% BSA, 25 mM HEPES pH 7.4 at 37 °C. NISV were resuspended by vortexing for 2 min in assay buffer to a final concentration of 0.375 mM. They were added to the apical (blood facing) side of the cells for 5 to 120 min on an orbital shaker (100 rpm) at 37 °C. For BBB transport studies, samples of the basal medium were then taken for analysis. For Astrocyte and PBEC cell uptake studies, cells were quickly washed with ice cold HBSS, lysed with 1% Triton-x 100 with EDTA-free protease inhibitors (Roche) for 30 min and samples taken. To investigate mechanisms of endocytosis or transcytosis, cells were pre-incubated for 30 min with the dynamin-mediated-endocytosis inhibitor Dynasore (80 μM) or Brefeldin A (5 μg/ml) to inhibit ER to Golgi exchange, or the assay was carried out at 4 °C to determine energy dependency. Cells for confocal microscopy were fixed in 4% paraformaldehyde for 45 min, washed with HBSS and stored in 70% glycerol until use.

4.15. Measurement of NISV and IgG cargo in in vitro assays

DiIC$_{18}$-labelled NISV and FITC-labelled IgG cargo, in samples of assay medium and cell lysate, were quantified using a CytoFluor fluorescent plate reader at 560/590 nm DiIC$_{18}$ and 485/520 nm for FITC (excitation/emission). For ease of comparison between the amount of NISV transported across the BBB with how much was taken up by endothelial PBEC cells or astrocytes, results are presented as % Dose *i.e.* the percentage of NISV added to the apical, blood-facing compartment that appears in the basal compartment (BBB transport), or within cell fractions (PBEC or astrocyte uptake). The amount of 'leaked'

versus encapsulated FITC-IgG cargo was measured in samples of apical and basal media. Samples were centrifuged at 14000 *g* for 5 min to pellet the NISVs with cargo, the supernatant aspirated to remove any leaked cargo, and samples assayed as described for FITC. The % leak is calculated from supernatant IgG-FITC/(supernatant + pellet) IgG-FITC).

4.16. Confocal microscopy

Imaging of cultured BBB and astrocyte cells was carried out on cells previously fixed with 4% paraformaldehyde on clear polyester Transwell filters (PBECs), or coverslips (astrocytes) in 12-well plates. All of the pre-fixed cells contained either or both of gNISV-DiIC$_{18}$ (red) and IgG-FITC (green). Cells were permeabilised with 0.1% Triton-x 100, incubated with either mouse monoclonal anti-Early Endosome 1 Antibody AlexaFluor 647, or Mouse monoclonal anti-58 K Golgi protein antibody AlexaFluor 647 or primary rabbit polyclonal anti-clathrin heavy chain antibody (1 in 200 dilution in DAKO blocking solution) followed by secondary Cy5 Goat Anti-Rabbit IgG (H + L) (1:100 dilution in DAKO). Separate cells were also stained either pre- or post-fixation with Wheat Germ Agglutinin to visualize cell membranes (CF640R or AlexaFluor 488 conjugates, 5 μg/ml). After staining, cells were mounted in Vectashield containing 4′,6-diamidino-2-phenylindole (DAPI) for nuclei staining. The Nikon A1 inverted confocal microscope was used with spectral detector and Eclipse Ti-E microscope at x40 or x100 (oil) magnification to generate digital images. Diode Laser wavelengths were set at 405 nm (DAPI), 488 nm (FITC), 561 nm (DiIC$_{18}$), 642 nm (Cy5/CR640). Image analysis was by Fiji (ImageJ).

4.17. Statistical analyses

A variety of statistical analyses have been performed using the program SPSS V21.0 (IBM) or Graphpad PRISM V6.0. Graphs have been constructed using Graphpad PRISM V6.0. Survival data were compared using log rank tests. Continuous data were analysed by parametric analysis (ANOVA, *t*-tests, GLM) when conditions were met (QQ plots to assess Gaussian distribution and Levene's/Bartlett tests for unequal variation) or non-parametric tests (Kruskal-Wallis, Mann-Whitney, Moods) where these criteria were not met. In some cases, it was possible for parametric criteria to be attained in the use of transformations such as logarithmic transformation. Contingency tables were used for binary data. Multiple testing corrections for familywise error were performed on individual comparisons with analyses. These included Bonferroni's and Dunn's corrections.

Author contributions

SW, EDW, CWR and RVD conceived the study and participated in its design. Formulation development and initial testing was carried out by SW with help from CWR. FJS carried out all histopathological analysis. LMO, WB, EDW and RVD carried out VEEV *in vivo* infection work. JEP, ARG, FM, and NJA conducted and interpreted the *in vitro* blood-brain barrier work. SW, JEP, EDW, CWR and RVD interpreted the results and wrote the manuscript. All authors read and approved the final manuscript.

Funding sources

This work was funded by the Defense Threat Reduction Agency (HDTRA1-12-D-0003-0014).

Acknowledgments

The authors would like to thank colleagues who facilitated the *in vivo* studies.

Appendix A. Supplementary data

Supplementary data to this article can be found online at https://doi.org/10.1016/j.jconrel.2020.05.048.

References

[1] N.J. Abbott, A.A.K. Patabendige, D.E.M. Dolman, S.R. Yusof, D.J. Begley, Structure and function of the blood-brain barrier, Neurobiol. Dis. 37 (2010) 13–25.
[2] S.A. Goodchild, L.M. O'Brien, J. Steven, M.R. Muller, O.J. Lanning, C.H. Logue, R.V. D'Elia, R.J. Phillpotts, S.D. Perkins, A humanised murine monoclonal antibody with broad serogroup specificity protects mice from challenge with Venezuelan equine encephalitis virus, Antivir. Res. 90 (2011) 1–8.
[3] L.M. O'Brien, S.A. Goodchild, R.J. Phillpotts, S.D. Perkins, A humanised murine monoclonal antibody protects mice from Venezuelan equine encephalitis virus, Everglades virus and Mucambo virus when administered up to 48 h after airborne challenge, Virology 426 (2012) 100–105.
[4] M. Bragagni, N. Mennini, C. Ghelardini, P. Mura, Development and characterization of niosomal formulations of doxorubicin aimed at brain targeting, J. Pharm. Pharm. Sci. 15 (2012) 184–196.
[5] A. Pardakhty, E. Moazeni, Nano-niosomes in drug, vaccine and gene delivery: a rapid overview, Nanomed. J. 1 (2013) 1–12.
[6] R.V. D'Elia, S. Woods, W. Butcher, J. McGahon, S. Khadke, Y. Perrie, E.D. Williamson, C.W. Roberts, Exploitation of the bilosome platform technology to formulate antibiotics and enhance efficacy of melioidosis treatments, J. Control. Release 298 (2019) 202–212.
[7] H. Abdelkader, A.W. Alani, R.G. Alany, Recent advances in non-ionic surfactant vesicles (niosomes): self-assembly, fabrication, characterization, drug delivery applications and limitations, Drug Deliv. 21 (2014) 87–100.
[8] M. Gharbavi, J. Amani, H. Kheiri-Manjili, H. Danafar, A. Sharafi, Niosome: a promising nanocarrier for natural drug delivery through blood-brain barrier, Adv. Pharmacol. Sci. 2018 (2018) 6847971.
[9] W.M. Pardridge, Molecular regulation of blood-brain barrier GLUT1 glucose transporter, in: J. Greenwood, D.J. Begley, M.B. Segal (Eds.), New Concepts of a Blood—Brain Barrier, Springer US, Boston, MA, 1995, pp. 81–88.
[10] W.A. Jefferies, M.R. Brandon, S.V. Hunt, A.F. Williams, K.C. Gatter, D.Y. Mason, Transferrin receptor on endothelium of brain capillaries, Nature 312 (1984) 162–163.
[11] P. Mergenthaler, U. Lindauer, G.A. Dienel, A. Meisel, Sugar for the brain: the role of glucose in physiological and pathological brain function, Trends Neurosci. 36 (2013) 587–597.
[12] C. Dufes, F. Gaillard, I.F. Uchegbu, A.G. Schätzlein, J.-C. Olivier, J.-M. Muller, Glucose-targeted niosomes deliver vasoactive intestinal peptide (VIP) to the brain, Int. J. Pharm. 285 (2004) 77–85.
[13] M. Bragagni, N. Mennini, S. Furlanetto, S. Orlandini, C. Ghelardini, P. Mura, Development and characterization of functionalized niosomes for brain targeting of dynorphin-B, Eur. J. Pharm. Biopharm. 87 (2014) 73–79.
[14] M. Hong, S. Zhu, Y. Jiang, G. Tang, Y. Pei, Efficient tumor targeting of hydroxycamptothecin loaded PEGylated niosomes modified with transferrin, J. Control. Rel. 133 (2009) 96–102.
[15] C. Dufès, M.A. Robaian, S. Somani, Transferrin and the transferrin receptor for the targeted delivery of therapeutic agents to the brain and cancer cells, Ther. Deliv. 4 (2013) 629–640.
[16] S.N. Gardner, K. McLoughlin, N.A. Be, J. Allen, S.C. Weaver, N. Forrester, M. Guerbois, C. Jaing, Characterization of genetic variability of Venezuelan equine encephalitis viruses, PLoS One 11 (2016) e0152604.
[17] F. Rivas, L.A. Diaz, M. Cardenas, E. Daza, L. Bruzon, A. Alcala, O. De la Hoz, F.M. Caceres, G. Aristizabal, J.W. Martinez, D. Revelo, F. De la Hoz, J. Boshell, T. Camacho, L. Calderon, V.A. Olano, L.I. Villarreal, D. Roselli, G. Alvarez, G. Ludwig, T. Tsai, Epidemic Venezuelan equine encephalitis in La Guajira, Colombia, 1995, J. Infect. Dis. 175 (1997) 828–832.
[18] P.V. Aguilar, J.G. Estrada-Franco, R. Navarro-Lopez, C. Ferro, A.D. Haddow, S.C. Weaver, Endemic Venezuelan equine encephalitis in the Americas: hidden under the dengue umbrella, Futur. Virol. 6 (2011) 721–740.
[19] E. Quiroz, P.V. Aguilar, J. Cisneros, R.B. Tesh, S.C. Weaver, Venezuelan equine encephalitis in Panama: fatal endemic disease and genetic diversity of etiologic viral strains, PLoS Negl. Trop. Dis. 3 (2009) e472.
[20] M.D. Cain, H. Salimi, Y. Gong, L. Yang, S.L. Hamilton, J.R. Heffernan, J. Hou, M.J. Miller, R.S. Klein, Virus entry and replication in the brain precedes blood-brain barrier disruption during intranasal alphavirus infection, J. Neuroimmunol. 308 (2017) 118–130.
[21] N. Forbes, M.T. Hussain, M.L. Briuglia, D.P. Edwards, J.H.T. Horst, N. Szita, Y. Perrie, Rapid and scale-independent microfluidic manufacture of liposomes entrapping protein incorporating in-line purification and at-line size monitoring, Int. J. Pharm. 556 (2019) 68–81.
[22] S. Moghassemi, A. Hadjizadeh, Nano-niosomes as nanoscale drug delivery systems: an illustrated review, J. Control. Rel. 185 (2014) 22–36.
[23] J. Li, P. Cai, A. Shalviri, J.T. Henderson, C. He, W.D. Foltz, P. Prasad, P.M. Brodersen, Y. Chen, R. DaCosta, A.M. Rauth, X.Y. Wu, A multifunctional polymeric nanotheranostic system delivers doxorubicin and imaging agents across the blood-brain barrier targeting brain metastases of breast cancer, ACS Nano 8 (2014) 9925–9940.
[24] R.E. Durand, P.L. Olive, Cytotoxicity, mutagenicity and DNA damage by Hoechst 33342, J. Histochem. Cytochem. 30 (1982) 111–116.

[25] Y. Kubo, S. Ohtsuki, Y. Uchida, T. Terasaki, Quantitative determination of luminal and abluminal membrane distributions of transporters in porcine brain capillaries by plasma membrane fractionation and quantitative targeted proteomics, J. Pharm. Sci. 104 (2015) 3060–3068.
[26] S.M. Ferguson, P. De Camilli, Dynamin, a membrane-remodelling GTPase, Nat. Rev. Mol. Cell Biol. 13 (2012) 75–88.
[27] H.B. Haimes, R.J. Stockert, A.G. Morell, A.B. Novikoff, Carbohydrate-specified endocytosis: localization of ligand in the lysosomal compartment, Proc. Natl. Acad. Sci. U. S. A. 78 (1981) 6936–6939.
[28] P. Ballabh, A. Braun, M. Nedergaard, The blood-brain barrier: an overview: structure, regulation, and clinical implications, Neurobiol. Dis. 16 (2004) 1–13.
[29] W.M. Pardridge, Brain drug development and brain drug targeting, Pharm. Res. 24 (2007) 1729–1732.
[30] J.C. Olivier, Drug transport to brain with targeted nanoparticles, NeuroRx 2 (2005) 108–119.
[31] E.A. Neuwelt, D.L. Goldman, S.A. Dahlborg, J. Crossen, F. Ramsey, S. Roman-Goldstein, R. Braziel, B. Dana, Primary CNS lymphoma treated with osmotic blood-brain barrier disruption: prolonged survival and preservation of cognitive function, J. Clin. Oncol. 9 (1991) 1580–1590.
[32] C.T. Curley, N.D. Sheybani, T.N. Bullock, R.J. Price, Focused ultrasound immunotherapy for central nervous system pathologies: challenges and opportunities, Theranostics 7 (2017) 3608–3623.
[33] A.R. Jones, E.V. Shusta, Blood-brain barrier transport of therapeutics via receptor-mediation, Pharm. Res. 24 (2007) 1759–1771.
[34] C. Dufes, J.M. Muller, W. Couet, J.C. Olivier, I.F. Uchegbu, A.G. Schatzlein, Anticancer drug delivery with transferrin targeted polymeric chitosan vesicles, Pharm. Res. 21 (2004) 101–107.
[35] K. Ulbrich, T. Knobloch, J. Kreuter, Targeting the insulin receptor: nanoparticles for drug delivery across the blood-brain barrier (BBB), J. Drug Target. 19 (2011) 125–132.
[36] S. Wagner, A. Zensi, S.L. Wien, S.E. Tschickardt, W. Maier, T. Vogel, F. Worek, C.U. Pietrzik, J. Kreuter, H. von Briesen, Uptake mechanism of ApoE-modified nanoparticles on brain capillary endothelial cells as a blood-brain barrier model, PLoS One 7 (2012) e32568.
[37] N. Bien-Ly, Y.J. Yu, D. Bumbaca, J. Elstrott, C.A. Boswell, Y. Zhang, W. Luk, Y. Lu, M.S. Dennis, R.M. Weimer, I. Chung, R.J. Watts, Transferrin receptor (TfR) trafficking determines brain uptake of TfR antibody affinity variants, J. Exp. Med. 211 (2014) 233–244.
[38] S. Mayor, R.G. Parton, J.G. Donaldson, Clathrin-independent pathways of endocytosis, Cold Spring Harb. Perspect. Biol. 6 (2014).
[39] S. Xu, B.Z. Olenyuk, C.T. Okamoto, S.F. Hamm-Alvarez, Targeting receptor-mediated endocytotic pathways with nanoparticles: rationale and advances, Adv. Drug Deliv. Rev. 65 (2013) 121–138.
[40] A.P.A. Ferreira, E. Boucrot, Mechanisms of carrier formation during clathrin-independent endocytosis, Trends Cell Biol. 28 (2018) 188–200.
[41] M. Mueckler, B. Thorens, The SLC2 (GLUT) family of membrane transporters, Mol. Asp. Med. 34 (2013) 121–138.
[42] C. Machut-Binkowski, F. Hapiot, R. Cecchelli, P. Martin, E. Monflier, A versatile liposome/cyclodextrin supramolecular carrierfor drug delivery through the blood-brain barrier, J. Incl. Phenom. Macrocycl. Chem. 57 (2007) 567–572.
[43] A.E. LaBauve, T.E. Rinker, A. Noureddine, R.E. Serda, J.Y. Howe, M.B. Sherman, A. Rasley, C.J. Brinker, D.Y. Sasaki, O.A. Negrete, Lipid-coated Mesoporous silica nanoparticles for the delivery of the ML336 antiviral to inhibit encephalitic alphavirus infection, Sci. Rep. 8 (2018) 13990.
[44] A.C. Guyton, Measurement of the respiratory volumes of laboratory animals, Am. J. Physiol. 150 (1947) 70–77.
[45] S.S.E. Nielsen, P. Siupka, A. Georgian, J.E. Preston, A.E. Toth, S.R. Yusof, N.J. Abbott, M.S. Nielsen, Improved method for the establishment of an in vitro blood-brain barrier model based on porcine brain endothelial cells, J. Vis. Exp. 127 (2017) e56277.